7.12 Projections $g_\theta(R)$ are taken of a unit square where $f(x, y) = \text{rect}\,(x)\,\text{rect}\,(y)$.
(a) Find a general expression for $g_\theta(R)$ and the particular functions for $\theta = 0°$ and 45°.
(b) Using the method of filtered back projection, find the *Fourier transform* of the back-projected function for the general case and for $\theta = 0°$ and 45°.

7.13 In the convolution back projection reconstruction system, find a general expression for the impulse response of the reconstruction $h(r)$ for a convolution function $c(R)$. The answer can be left in integral form and should be a function of r and R only.

8

Nuclear Medicine

In radiography the regions under study are used in a transmission mode in the measurement of the attenuation coefficient. This measurement is often enhanced by the selective administration of radiopaque contrast materials. In nuclear medicine [Blahd, 1965] the region under study becomes an active source. This is done through the selective administration of radioactive materials since the body contains no natural radioactive substances. Either the radioactive material itself, or the chemical form it is bound in, has properties that cause it to be selectively taken up in specific regions of the anatomy. Once taken up in the organs of interest, these become radiating sources. Thus the imaging problem in nuclear medicine is that of defining a three-dimensional source distribution rather than a distribution of attenuation coefficients.

It is important to point out that, in general, much smaller amounts of administered materials are required in nuclear medicine than in radiographic contrast studies. The radiation dose problems are also quite different. In radiography the patient is irradiated only during the time the x-ray beam is turned on. In nuclear medicine the patient is being irradiated from the moment the radioactive material is administered until it is either eliminated by the body or decays.

The earliest nuclear medicine studies were made on the thyroid gland by taking advantage of its natural affinity for iodine. An isotope of iodine ^{131}I was used as the tracer material. This emits gamma rays at an energy of 364 kev.

Gamma rays are photons having the same energy range as x-rays. The definition simply distinguishes their source, with x-rays generated by electron events and gamma rays generated by nuclear events. The energy of 364 kev is somewhat high by radiography standards. In nuclear medicine, however, attenuation of the photons is undesirable. The requirement for negligible attenuation would of itself suggest very high energy isotopes. However, this requirement is moderated by the imaging considerations. Obtaining good collimation and efficient detection is difficult at very high energies, so that the energies used are often a compromise between the attenuation and imaging requirements.

In recent years ^{99m}Tc, an isotope of technicium [Blahd, 1965], has gotten wide acceptance as the preferred material for a variety of studies. This decision is based primarily on three desired properties. First, it is relatively easily made by chemical generators rather than requiring a cyclotron. Second, it has a gamma-ray emission energy of 140 kev, which is a good compromise between body attenuation and imaging considerations. Third, it has a relatively short half-life of 6 hours, for low radiation dosage.

SCANNED DETECTORS

In the early thyroid studies the imaging device was a simple single-bore, lead collimator which was scanned over the area of interest as shown in Fig. 8.1. Photons passing through the hole gave up their energy in a scintillating crystal whose material is comparable to that used in *x*-ray screens. Materials such as sodium iodide are used with the resultant visible photons coupled to a photomultiplier tube where an electrical signal is created. The crystal is made relatively thick so as to capture the gamma rays with almost 100% quantum efficiency. The number of light photons produced per gamma-ray photon and the light quantum efficiency of the photocathode are sufficiently high so that the signal-to-noise ratio is dominated by the number of received gamma-ray photons. The detector is mechanically scanned across the area of interest. The resultant signal is used to intensity modulate a synchronously scanned display which produces an image of the radioactivity distribution. Some scanners use

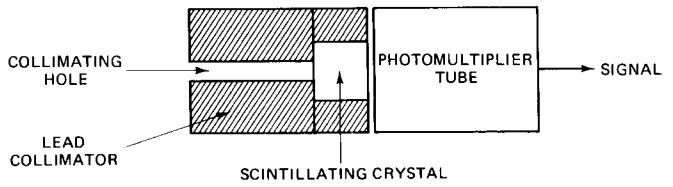

FIG. 8.1 Scanned gamma-ray detector.

focused collimators, aimed at a specific depth range, to provide a limited degree of depth resolution.

The relative radioactivity, often specified as representing hot and cold regions, is of diagnostic significance. In the thyroid these indicate regions of overactivity and underactivity. In other organs lesions can be demonstrated by regions of either underactivity or overactivity as compared to the normal organ. For example, brain tumors tend to localize the radioactive material and produce a hot spot. Liver studies, on the other hand, are produced by injecting a colloidal radioactive substance which is taken up in normal liver tissue. Thus regions of disease, such as tumors, are characterized by cold spots which do not take up the administered colloidal material.

Scanned systems are unsuitable for studying the dynamics of the functioning of an organ or system because of the long time required to view the area of interest. To accomplish this function cameras have been developed which view an entire region at once and make a series of images that indicate the distribution of the radioactive material at different time intervals. The ability to make these images rapidly is governed by the efficiency of the camera and the amount of radioactive material used. This amount is limited by radiation considerations.

The basic unit of activity is the curie (Ci), which is defined as 3.7×10^{10} disintegrating nuclei per second. In the case of a gamma-ray emitter this represents the number of photons emitted per second. The amount of radiation dose is thus determined by the amount administered, the half-life of the material, and the ability of the body to excrete the material. Iodine 131 is used in thyroid studies and has a half-life of 8.1 days. A dose of 25 μCi results in a radiation dose of 40 rad, a number significantly greater than any radiographic study. In the early days, using relatively inefficient detectors, doses of 50 to 250 μCi were used. With present-day detectors, doses of 5 μCi and less are used.

Scanned detector systems have rapidly declined in popularity, although they continue to be used for visualizing static structures of the body. This is particularly true of studies involving very large fields of view, such as a whole-body bone scan [Laughlin et al., 1960]. Figure 8.2 illustrates a commercial scanner together with a typical whole-body bone scan. As can be seen, the image is relatively noisy and of considerably lower resolution than typical radiographic images.

IMAGING CONSIDERATIONS WITH GAMMA-RAY CAMERAS

The gamma-ray camera allows an entire field to be studied simultaneously without requiring a mechanical scan. For both static and dynamic studies, these are rapidly becoming the most widely used instruments. A basic gamma-ray camera is shown in Fig. 8.3.

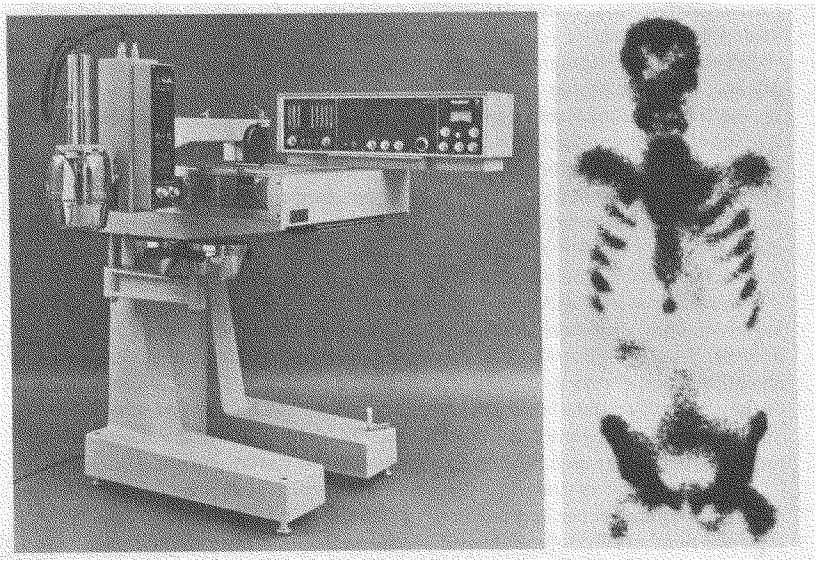

FIG. 8.2 Commercial scanner and a typical whole-body bone scan.

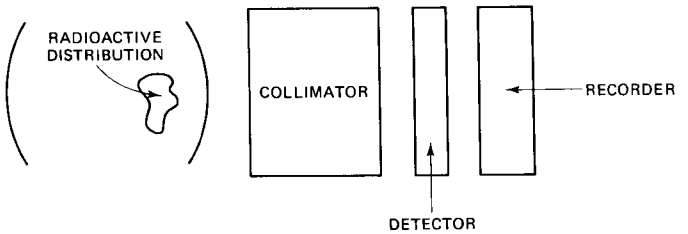

FIG. 8.3 Basic gamma-ray camera.

The camera consists of a collimator for forming the radioactive distribution into a two-dimensional image, a detector for detecting the position of each gamma-ray photon, and a recorder for producing an image from the detected photons. The detector considerations are similar to those of radiography. The material should be sufficiently thick and of high attenuation coefficient so as to stop most of the high-energy photons and produce large numbers of visible photons. A typical nuclear medicine detector has a $\frac{1}{2}$-inch-thick sodium iodide crystal.

The recorder must register the position of each event and form an image.

Film, the recorder used in radiography, is unsuitable because of scatter considerations. A large number of the emitted photons are Compton scattered and appear in the detector at erroneous positions. In radiography these are attenuated by collimating grids since we know which direction the desired rays are coming from. In nuclear medicine, the direction of the desired rays is unknown. Scatter discrimination is provided by making use of the nature of Compton scattering described in Chapter 3. Each scattered photon has a reduced photon energy. At the relatively high energies used in nuclear medicine isotopes, this energy change is significant enough to be measured. Also, the photon rate is sufficiently slow that individual photons can be distinguished. Each single photon captured in the detector produces a number of visible photons proportional to the energy of the gamma ray. Desired events can be distinguished from scattered events by the amplitude of the light pulse produced. Thus electronic recorders, such as an array of photomultipliers with pulse-height analyzers, can minimize the scattered radiation. This capability is unavailable using photographic film. In addition, having the signal in an electronic form makes possible a variety of processing, such as geometric distortion correction.

One generalized configuration for a detector and recorder utilizes an array of individual detectors. The output from each detector represents the integrated number of photons over a given incremental area. The detected outputs can be coupled to a recorder, where an image is produced of the intensity at the detector plane. Arrays of this form have been used employing scintillating crystals followed by photomultipliers [Bender and Blau, 1963]. In recent years suitable two-dimensional arrays have been built using gaseous multiwire proportional counters and also using cooled semiconductor arrays such as intrinsic and lithium-drifted silicon and germanium. In the detector arrays considered, the system resolution is limited to the number of discrete detectors used. With some detectors, such as sodium iodide scintillating crystals followed by photomultipliers, this can be a very awkward and expensive configuration if reasonable resolution is desired.

ANGER CAMERA

The Anger camera, named after its inventor, is a system for achieving a large number of resolvable elements with a limited number of detectors [Anger, 1958]. It thus overcomes the previous difficulty of having the resolution limited by the number of discrete detectors. The principle is based on estimating the position of a single event by measuring its contribution to a number of detectors. This system requires that the detector be capable of distinguishing individual events, no matter where they occur. Two simultaneous events occurring at different portions of the detector system would be rejected by this camera, whereas it could be recorded by the previously described array of individual detectors.

The basic principle is simply illustrated in Fig. 8.4 with a single slab of scintillating crystal followed by two photocells centered at x_1 and x_2. The light received from each detector, due to single events, is distributed among the two detectors based on the position of the event. Thus the position of the event $\bar{x}$ can be estimated as

$$\bar{x} \simeq \frac{I_1 x_1 + I_2 x_2}{I_1 + I_2}. \tag{8.1}$$

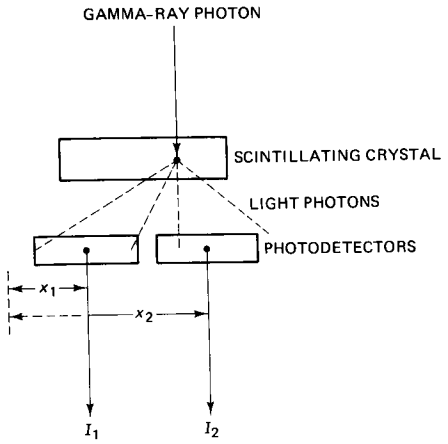

FIG. 8.4 Anger camera principle.

The ultimate resolution in the x direction, using only two detectors, is determined by the accuracy of the formula and, more important, the statistics of each measurement rather than by the size or number of detector elements. It must be emphasized, however, that the process requires detecting single events. If more than one scintillation takes place during the measurement interval, the position cannot be determined. Fortunately, the $I_1 + I_2$ sum can be used to indicate the sum of the counts received so as to discard multiple events and scatter. Cameras of this general type have a single crystal viewed by arrays of detectors with the detected outputs followed by a position computer to estimate the position of each event.

A typical detector system of this type is shown in Fig. 8.5. The light from the crystal is divided among the photomultiplier tubes arranged in a hexagonal array. The sum of the outputs is used for energy selection to achieve scatter rejection. If the pulse height fails to fall within prescribed limits for the isotope used, the pulse is rejected by blanking the intensity of the display device. This same process also rejects occasional multiple events. The position of the event

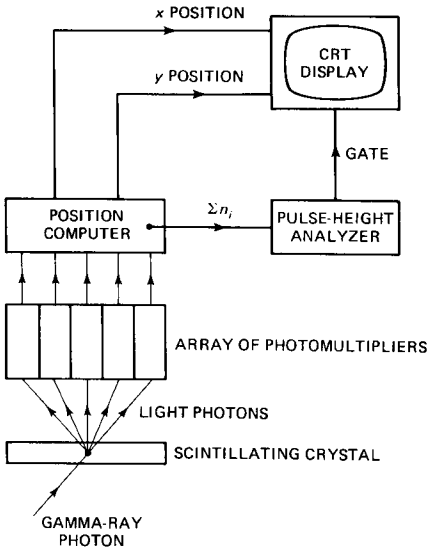

FIG. 8.5 Block diagram of an Anger camera.

on the crystal is determined by a centroid calculation. The estimate of the x and y coordinates of the event, $\hat{x}$ and $\hat{y}$, are given by

$$\hat{x} = \frac{\sum_i x_i n_i}{\sum_i n_i} \tag{8.2}$$

and

$$\hat{y} = \frac{\sum_j y_j n_j}{\sum_j n_j} \tag{8.3}$$

where x_i and y_j are the x and y coordinates of the center of the photomultipliers and n_i and n_j are the number of light photon counts or the pulse amplitudes in each photomultiplier. This system provides a resolution of over 1000 resolvable elements using 19 photodetectors. This is made possible by analyzing single events. However, even the 1000 elements represent a lateral resolution of about 1 cm, considerably less than that used in radiography.

The resolution of the camera, rather than depending on the number of discrete detectors, is determined by the accuracy of the position computation. This is limited by the counting statistics of the number of light photons at each photomultiplier. In calculating the statistics of the position measurement we make the simplifying assumption that the total number of collected counts $\sum_i n_i$ is a constant equal to N. First, with a large number of counts, the statistical

variation in this quantity will be small compared to that of each n_i. Second, the pulse-height analysis will reject events whose total count is not in the immediate vicinity of N. The expected value of $\hat{x}$ is therefore given by

$$E(\hat{x}) = \frac{1}{N}\sum_i x_i E(n_i)$$

$$= \sum_i x_i \frac{\Omega_i}{\sum_j \Omega_j} \tag{8.4}$$

where Ω_i is the solid angle subtended by the ith photomultiplier from the light emitted from the scintillating crystal at point x, y and $\Omega_i/\sum_j \Omega_j$ is the fraction of the total collected counts in the ith photomultiplier. The solid angle at each photomultiplier due to an event at x, y can be approximated as

$$\Omega_i \simeq \frac{Ad}{[(x_i - x)^2 + (y_i - y)^2 + d^2]^{3/2}} \tag{8.5}$$

where A is the area of the photomultiplier cathode and d is the z distance from the event to the photocathodes. The distance d is assumed constant since the thickness of the crystal is smaller than the distance from the crystal to the photomultipliers as shown in Fig. 8.5.

The variance of the measurement, which determines the accuracy, is given by

$$\text{var}\,\hat{x} = \sum_i \left(\frac{x_i}{N}\right)^2 \text{var}\, n_i$$

$$= \sum_i \frac{x_i^2}{N} \frac{\Omega_i}{\sum_i \Omega_i}. \tag{8.6}$$

The standard deviation of the computation is therefore

$$\sigma_{\hat{x}} = \left\{\frac{1}{N} \frac{\sum_i x_i^2[(x_i - x)^2 + (y_i - y)^2 + d^2]^{-3/2}}{\sum_j [(x_j - x)^2 + (y_j - y)^2 + d^2]^{-3/2}}\right\}^{1/2} \tag{8.7}$$

where the area of the photomultiplier A cancels out. This area determines the overall collection efficiency which governs N, the total number of counts, as given by

$$N = \eta_p \frac{\lambda_{\text{light}}}{\lambda_{\text{x-ray}}} \frac{\sum_i \Omega_i}{4\pi} \tag{8.8}$$

where η_p is the efficiency of light production of the scintillating material. The calculations are essentially identical for $\sigma_{\hat{y}}$.

In Table 8.1 we list the standard deviation for a number of cases. For simplicity, a square $L \times L$ array of contiguous square photodetectors has been used. The spatial resolution or number of elements along each axis can be approximated by $L/2\sigma_{\hat{x}}$, with the total number of resolvable elements being the square of that number. A total number of 1000 collected photons is assumed for N. As shown in Table 8.1, the accuracy increases as the number of photomultipliers increase. The accuracy for points on the axis is improved by decreasing the distance d from the photodetectors to the scintillator. However, for off-axis sources the accuracy deteriorates at a more rapid rate for the smaller d. Also, a smaller field of view provides improved accuracy at the price of viewing a limited portion of the anatomy.

TABLE 8.1

PERFORMANCE OF ANGER CAMERA

x, y Position of Source (cm)	Array Size, L (cm)	Photomultiplier Size (cm)	Total Number of Photomultipliers	Detector to Scintillator Distance d (cm)	Standard Deviation (cm)
0, 0	40	4	100	5	0.225
0, 0	40	8	25	5	0.25
0, 0	40	8	25	3	0.224
0, 0	40	4	100	3	0.177
20, 20	40	4	100	3	0.578
20, 20	40	8	25	3	0.614
20, 20	40	8	25	5	0.578
10, 10	40	8	25	3	0.368
0, 0	20	4	25	3	0.131
5, 5	20	4	25	3	0.186
10, 10	20	4	25	3	0.28

It should be emphasized that the centroid calculation of the position given in equations (8.2) and (8.3) are not optimum from a statistical point of view. The uniform weighting given each measurement can be shown to be suboptimal. Newer forms of position arithmetic [Gray and Macovski, 1976] using nonuniform weightings of the measurements are being used to provide reduced standard deviations for a given photon count.

PINHOLE IMAGING STRUCTURES

The imaging portion or collimator of the camera system in Fig. 8.3 contributes significantly to the determination of the efficiency and the lateral resolution. Radiographic systems do not need an imaging structure since the transmitted photons define the image through shadowing. In nuclear medicine we are imaging the source and thus require an imaging or collimating structure. Lenses are unavailable at this energy range since the refractive index of all transparent materials is unity. Since only attenuation mechanisms are available, a pinhole becomes the logical imaging device. This is known in nuclear medicine as a pinhole collimator and is shown in Fig. 8.6.

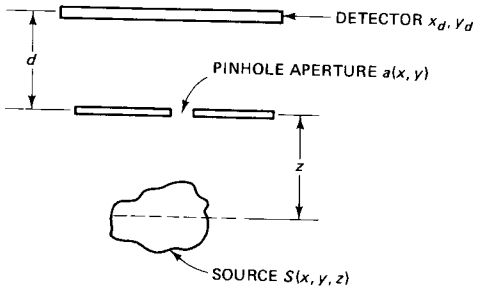

FIG. 8.6 Pinhole imaging system.

If the pinhole were an infinitesimally small opening on the axis of the system, a planar source at z, $S(x, y)$, would be reproduced at the detector plane as

$$I_d(x_d, y_d) = KS\left(\frac{x_d}{M}, \frac{y_d}{M}\right) \tag{8.9}$$

where the magnification M is given by

$$M = -\frac{d}{z}. \tag{8.10}$$

Although this system would have perfect fidelity in lateral resolution, it would have zero intensity since K, which is determined by the solid angle of interception, would approach zero.

To provide adequate photon flux the pinhole is opened to an aperture $a(x, y)$. We make the assumption that the aperture plate is infinitesimally thin and is completely opaque to the emitted gamma rays. Although this combination of assumptions is somewhat inconsistent, it does make the system space invariant and allows us to place the detected output in a convenient convolutional form. An aperture plate of finite thickness will have a space-variant point response because the sides of the aperture will alter its effective size when viewed from different angles.

To calculate the impulse response we place a single photon point source at x, y, z. The intensity or photon density at the detector plane due to photons entering the aperture, using the same development as given in equations (4.2) to (4.5), is $[1/4\pi(z + d)^2] \cos^3 \theta$, where θ is the angle the rays make with the normal. The extent of this intensity pattern is the magnified projected aperture function projected from the point source. This magnified image of the aperture is translated by Mx and My, respectively, where M is the image magnification $-d/z$. Thus the impulse response at the detector due to a point source is given by

$$h(x, y, x_d, y_d) = \frac{\cos^3 \theta}{4\pi(z + d)^2} a\left(\frac{x_d - Mx}{m}, \frac{y_d - My}{m}\right) \tag{8.11}$$

where m is the magnification of the projected aperture as given by

$$m = \frac{z + d}{z} = 1 - M. \tag{8.12}$$

In the interest of providing a space-invariant impulse response, with a subtle loss in accuracy, we ignore the $\cos^3 \theta$ dependence of the oblique rays. Since the system is linear we use the superposition integral to find the output $I_d(x_d, y_d)$ due to a general planar source $S(x, y)$ at plane z as given by

$$I_d(x_d, y_d) = \frac{1}{4\pi(z + d)^2} \int\int S(x, y) a\left(\frac{x_d - Mx}{m}, \frac{y_d - My}{m}\right) dxdy. \tag{8.13}$$

The previous approximation, which neglected the finite thickness of the pinhole aperture, and the $\cos^3 \theta$ obliquity factor have enabled us to structure this expression in convolutional form. We do this by making the substitutions

$$x' = Mx \quad \text{and} \quad y' = My$$

giving

$$I_d(x_d, y_d) = \frac{1}{4\pi d^2 m^2} S\left(\frac{x_d}{M}, \frac{y_d}{M}\right) ** a\left(\frac{x_d}{m}, \frac{y_d}{m}\right). \tag{8.14}$$

The capture efficiency of the system is simply based on the solid collection angle Ω. Using the same simplifying approximations used in developing the impulse response, we have

$$\eta(z) = \frac{\Omega}{4\pi} \simeq \frac{\int\int a(x, y)\, dxdy}{4\pi z^2} = \frac{A_p}{4\pi z^2}. \tag{8.15}$$

Here we see the basic trade-off between efficiency and resolution as represented by the area A_p of the pinhole.

It is instructive to examine equation (8.14) to evaluate the intensity of the image as a function of depth. If the source is a small point, the intensity of the image will decrease with increasing depth as indicated by the $(z + d)^2$ factor in the denominator of (8.11). Thus, as the point source is moved farther away, the projected aperture image will become both smaller and less intense.

The situation is different, however, for a large extended source whose lateral extent is appreciably greater than the extent of the projected aperture. Although the resolution and the magnification of the image vary with depth, the resultant intensity is depth independent. This can be appreciated by noting that the area of $a(x/m, y/m)/m^2$ is equal to A_p for all m. Essentially, the z dependence in $\eta(z) = A_p/4\pi z^2$ is canceled by that of $M^2 = d^2/z^2$. Thus the detected photon density due to a broad area source at some plane z is independent of the distance z from the pinhole. This can be appreciated if we consider the photons collected by a point on the detector plane. As the source plane moves away, corresponding to increasing z, the collection efficiency goes down, but the source area seen by the point increases. These conflicting phenomena cancel and result in a z independence within the paraxial approximation. In general, with in-

creasing z, the detected image becomes smaller as the photon efficiency decreases, maintaining the photon density.

The impulse response of equation (8.11) and the resultant intensity of equation (8.13) could also have been derived using the "alternative analysis using planar object" described in Chapter 4. As shown in Fig. 4.13, the response due to an impulsian pinhole can be formulated as in equation (4.37). The system impulse response is then derived by integrating over the entire aperture function. The desired system response is obtained by substituting the source distribution $S(x, y)$ for the x-ray source $s(x, y)$ and substituting the aperture function $a(x, y)$ for the transmission $t(x, y)$. The magnification constants m and M must be appropriately defined to achieve the desired result.

We have considered the intensity due to a specific plane. For the general case consisting of a volumetric source the resultant image is the linear superposition of the contribution due to all z planes in $S(x, y, z)$. The total integrated intensity is given by

$$I_d(x_d, y_d) = \frac{1}{4\pi d^2} \int \frac{1}{m(z)^2} \left[S\left(\frac{x_d}{M(z)}, \frac{y_d}{M(z)}, z\right) ** a\left(\frac{x_d}{m(z)}, \frac{y_d}{m(z)}\right) \right] dz. \quad (8.16)$$

This result is distinctly different from that of projection radiography, where the volumetric object resulted in the nonlinear relationships of (4.41) and (4.42). In those cases it was necessary to use various approximations to linearize the system and allow the use of convolutional forms.

Equation (8.16) has neglected the effects of the attenuation of the object. In general, each radiating source experiences the attenuation of the tissue before reaching the detector. Although the attenuation is relatively low at the high energies used, its effects can be considerable. One simplified approach is to assume that the tissue attenuation is a constant, equal to that of water. In that case, knowing the approximate outline of the region being studied, we can make a good estimate of the attenuation effect. For example, if the factor $e^{-\mu(z-z')}$ is included in equation (8.16), it will provide a significant attenuation correction. Here μ is the average attenuation coefficient of water or tissue at the energy used and z' is the distance of the border of the patient from the pinhole.

The size of the aperture represents a fundamental trade-off between resolution and efficiency. The total number of received photons is proportional to A_p. Assume that it is desired to improve the system resolution by reducing the linear size of a resolution element by a factor of 2. Since the number of elements in the detector has increased by four, four times as many detected photons are required to obtain the same statistics in each picture element. To improve the resolution of the imaging structure the width of the pinhole is halved, reducing the photon efficiency η by 4. Therefore, a 16: 1 increase in the number of emitted photons are required to halve the linear size of a picture element. Thus the photon requirement varies as the fourth power of the linear resolution.

This fourth-power variation of the emitted photons with the linear dimensions of the aperture can be again seen by studying equation (8.14). This

equation represents intensity or photons per unit area. If multiplied by the projected pinhole area, $m^2 A_p$, it will represent photons per element. The projected source $S(x/M, y/M)$ is therefore multiplied by A_p and convolved with the aperture function whose area is A_p. The required number of emitted photons, for a given number of photons per element, is therefore inversely proportional to A_p^2 or the fourth power of the linear extent of the aperture $a(x, y)$.

One significant difficulty with pinhole collimators is that the image magnification M varies inversely with depth. This can be significant in that lesions of unknown depth can appear with arbitrary magnification. This can be important in nuclear medicine, where there are few anatomical guidelines so that spatial distortions in an apparent lesion can be more serious. It is not apparent, therefore, whether a small image represents a small lesion or a large distant lesion. As a result of this deficiency, pinhole collimators are normally used for viewing organs at known depths such as the thyroid gland. They are rarely used for inspecting a volume, such as the head, for tumors that might occur anywhere in the space. A photograph of a commercial pinhole collimator together with a typical thyroid image are shown in Fig. 8.7.

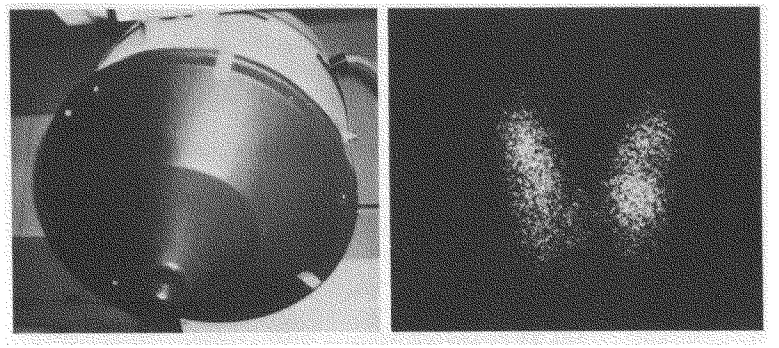

FIG. 8.7 Pinhole collimator and a thyroid image made with the collimator.

PARALLEL HOLE COLLIMATOR

The parallel hole collimator [Anger, 1964] shown in Fig. 8.8 overcomes some of the problems of the pinhole collimator. In essence this structure is an attempt at collimating the emitted radiation so as to record an image having unity magnification at all depth planes. The region being studied is placed against the collimator so as to get all of the sources as close as possible. Unlike the pinhole the magnification does not vary with depth and is a constant at unity.

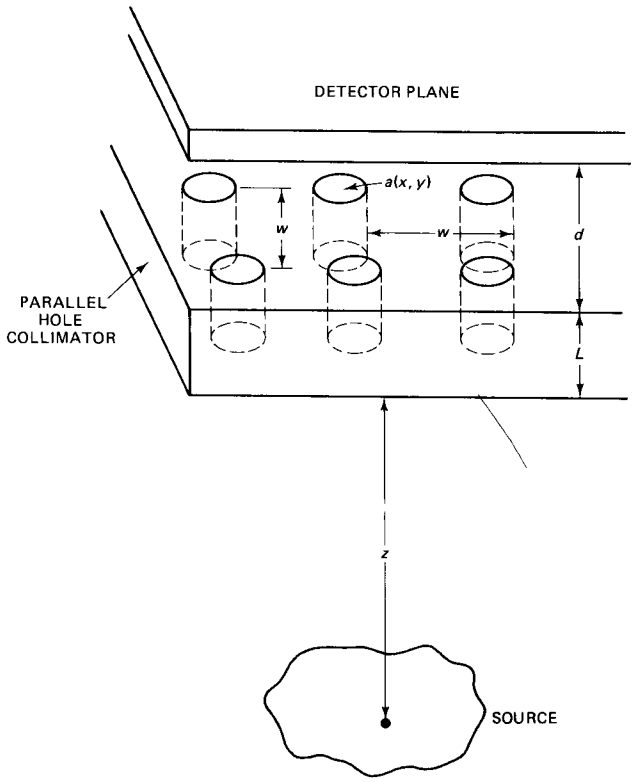

FIG. 8.8 Parallel-hole collimator imaging system.

As shown in Fig. 8.8, the parallel hole collimator is a block of high attenuation material, usually lead, with an array of spaced parallel holes each having an opening $a(x, y)$ and whose centers are separated by w in the x and y dimensions. The three-dimensional attenuation coefficient can be modeled as

$$\mu(x, y, z) = \mu_0\left[1 - a(x, y) ** \text{comb}\left(\frac{x}{w}\right)\text{comb}\left(\frac{y}{w}\right)\right]\text{rect}\left(\frac{z + L/2}{L}\right). \quad (8.17)$$

In general each hole of the collimator is responsive primarily to activity in its vicinity. This accounts for the unity magnification.

For a more detailed analysis we employ the general method suggested by Metz et al. [1980], where the collimator material is assumed to be perfectly

opaque. We then explore the geometric projection of point sources at various positions through the holes. It is evident, observing Fig. 8.8, that this will lead to a space-variant formulation. Clearly, the response will be different for a point centered directly below a hole than one centered in a septal region between holes. Space-variant responses, although accurate, have questionable value in systems analysis since they do not result in convolutional forms, nor do they provide transfer functions in the frequency domain. For these reasons we use the concept of averaged responses as suggested in the Metz et al. paper. Since each source has uniform probability of being at each x, y position, we provide an inpulse response averaged over collimator position which is space invariant and has the desired properties.

The calculation of the impulse response is similar to that of the pinhole collimator except for the finite thickness of the collimator. The result is similar to that of equations (4.5) through (4.10), where μ_0 approaches infinity. This represents the rays reaching the detector which are not obscured by the collimator material. When the point source is at or near a region corresponding to the center of a hole, the impulse is simply the projection of the back aperture function nearest the detector, a magnified version of $a(x, y)$. As the point moves laterally, the rays begin to be obscurred by the front aperture function nearest the source, which has a larger magnification. The resultant response is the product of the two projections, as illustrated in Fig. 8.9.

Figure 8.9 shows the projection for a single on-axis hole. Photons can reach the detector only at the intersection of the projections of the back and front apertures. In studying the systems response we use the same notation as that of the pinhole collimator, where m is the magnification of the projection of the hole and M is the lateral magnification of the source position. It must be emphasized, however, that these magnifications are used solely in developing the system response. Clearly, the overall system magnification will be unity. Using the subscript 1 for the back aperture and 2 for the front aperture, we have

$$m_1 = \frac{z + L + d}{z + L} \quad (8.18)$$

$$m_2 = \frac{z + L + d}{z} \quad (8.19)$$

and

$$M_1 = -\frac{d}{z + L} \quad (8.20)$$

$$M_2 = -\frac{d + L}{z}. \quad (8.21)$$

For notational convenience, let the lateral aperture function in equation (8.17) be given by

$$b(x, y) \quad a(x, y) ** \text{comb}\left(\frac{x}{w}\right)\text{comb}\left(\frac{y}{w}\right). \quad (8.22)$$

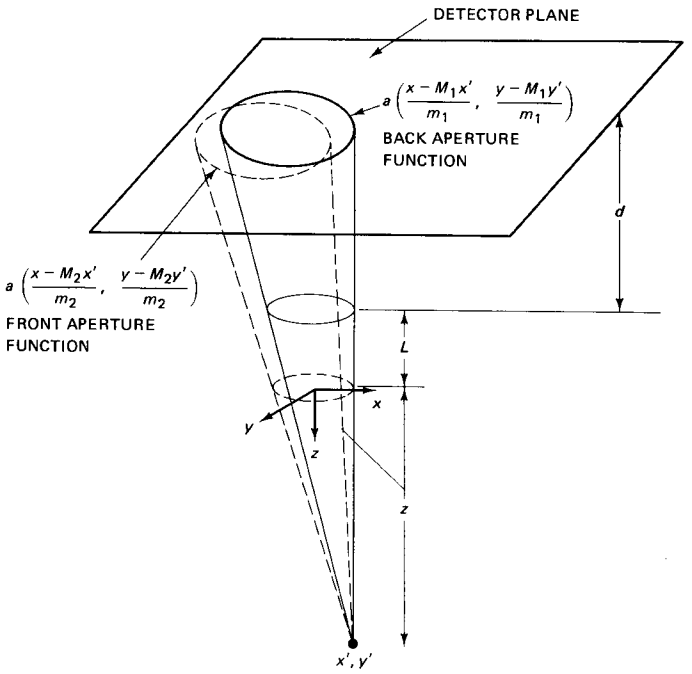

FIG. 8.9 Projection of a single-on-axis hole.

Using this notation the response at detector coordinates x_d, y_d to an impulse at x', y' at a depth z is given by

$$h(x_d, y_d, x', y') = \frac{\cos^3\theta}{4\pi(z+L+d)^2} b\left(\frac{x_d - M_1x'}{m_1}, \frac{y_d - M_1y'}{m_1}\right) \times b\left(\frac{x_d - M_2x'}{m_2}, \frac{y_d - M_2y'}{m_2}\right) \quad (8.23)$$

where, as before, θ is the obliquity angle of the rays from the normal. We again make the simplifying assumption that θ is sufficiently small to ignore $\cos^3\theta$. This represents a stronger, more accurate, assumption than that of the pinhole collimator since only rays having small angles to the normal can penetrate a parallel hole collimator because of its thickness.

The impulse response of (8.23) is clearly space variant and cannot conveniently be used to find the image due to a general source distribution. Also, the affect of the collimator in the frequency domain cannot be studied. The space variance can be seen mathematically in that no change of variables can reduce

the expression to represent the difference of input and output coordinates. This is confirmed physically in studying Fig. 8.9 in that different source positions produce different intersections of the projections of the front and back aperture functions.

As indicated, we will attempt to develop an average impulse response. In effect, we will move the collimator such that the origin moves over a period from $-w/2$ to $w/2$ in x and y and integrate the result. Our averaged impulse response is therefore

$$\bar{h}(x_d, y_d, x', y') = \frac{\frac{1}{w^2}\int_{-w/2}^{w/2}\int b\left(\frac{x_d - M_1x' - m_1x}{m_1}, \ldots\right) b\left(\frac{x_d - M_2x' - m_2x}{m_2}, \ldots\right) dxdy}{4\pi(z+L+d)^2} \quad (8.24)$$

where the y dependence in each expression for b is identical to that of x and has been omitted for brevity. Equation (8.24) can be structured into a convenient autocorrelation form using the substitutions

$$p = \frac{x_d}{m_1} - \frac{M_1}{m_1}x' - x, \qquad q = \frac{y_d}{m_1} - \frac{M_1}{m_1}y' - y \quad (8.25)$$

resulting in

$$\bar{h}(x_d, y_d, x', y') = \frac{1}{4\pi(z+L+d)^2w^2}\int_{-w/2}^{w/2}\int b(p, q) \times b\left[p + \frac{L}{z+L+d}(x_d - x'), q + \frac{L}{z+L+d}(y_d - y')\right] dpdq \quad (8.26)$$

$$= \frac{1}{4\pi(z+L+d)^2w^2}\Gamma_b\left[\frac{L}{z+L+d}(x_d - x', y_d - y')\right] \quad (8.27)$$

where $\Gamma_b(c, d)$ is the two-dimensional autocorrelation evaluated at c, d defined as

$$\Gamma_b(c, d) = \int_{-w/2}^{w/2}\int b(p, q)b(p + c, q + d)\, dpdq. \quad (8.28)$$

Equation (8.27) clearly illustrates the averaged space-invariant impulse response. Since the impulse response is directly proportional to the difference between the source and detector coordinates the system has unity magnification.

The derivation was based on the lateral aperture function $b(x, y)$ in equation (8.22), consisting of a regular array of apertures $a(x, y)$. It is interesting to note that, under typical conditions, the intersection of the two aperture functions, as given in equations (8.24) and (8.26), includes just a single aperture. That is, a point source will produce an image only due to the single hole it is under, and none other. As we translate a point source from the axis, the area of overlap of the front- and back-projected aperture functions becomes less and less until it is zero. If the amount of translation at that point is less than $w/2$, half the dis-

tance between holes, then the point clearly cannot project through other holes. If it exceeds $w/2$, the impulse response will involve a number of holes.

If D represents the lateral extent of the hole $a(x, y)$, the condition for the impulse response to be based on a single aperture is given by

$$w > \frac{D(m_1 + m_2)}{M_1 - M_2} \tag{8.29}$$

corresponding to a depth range

$$z < \frac{L(w - D)}{2D}. \tag{8.30}$$

For most parallel hole collimators, typical depths will be within this range. Therefore, the average impulse response becomes

$$\bar{h}(x_d, y_d) = \frac{1}{4\pi(z + L + d)^2 w^2} \Gamma_a\left(\frac{L}{z + L + d} x_d, \frac{L}{z + L + d} y_d\right) \tag{8.31}$$

where Γ_a is the autocorrelation of the aperture $a(x, y)$. Using this impulse response, the intensity due to a general source distribution $S(x, y, z)$ is given by

$$I_d(x_d, y_d) = \int \frac{1}{4\pi(z + L + d)^2 w^2} \times \left[\Gamma_a\left(\frac{L}{z + L + d} x_d, \frac{L}{z + L + d} y_d\right) ** S(x_d, y_d, z)\right] dz. \tag{8.32}$$

It must be recalled that this detected intensity is based on an averaged impulse response which would occur if the collimator were scanned during the exposure. It also represents the estimated impulse response of this space-variant system.

The efficiency is determined in the same way with the average efficiency $\bar{\eta}$ determined by the average projection area as given by

$$\bar{\eta} = \frac{1}{4\pi(z + L + d)^2 w^2} \int\int \Gamma_a\left(\frac{L}{z + L + d} x_d, \frac{L}{z + L + d} y_d\right) dx_d dy_d. \tag{8.33}$$

Using the average impulse response we can develop a transfer function $\mathfrak{A}(u, v)$ using the fact that the Fourier transform of an autocorrelation is the squared magnitude of the function's transform. The transfer function is given by

$$\mathfrak{A}(u, v) = \mathfrak{F}\{\bar{h}(x_d, y_d)\} = \frac{1}{4\pi L^2 w^2} \left| A\left(\frac{z + L + d}{L} u, \frac{z + L + d}{L} v\right)\right|^2 \tag{8.34}$$

where $A(u, v)$ is the transform of the aperture function $a(x, y)$. This transfer function can be used to find the response due to any planar source as given by

$$I_d(u, v) = \mathfrak{A}(u, v) S(u, v) \tag{8.35}$$

where $S(u, v)$ is the Fourier transform of a planar source distribution $S(x, y)$.

NOISE CONSIDERATIONS

The noise considerations in nuclear medicine imaging are dominated by the Poisson statistics of the relatively few detected photons. Scatter is an additional noise source because of the limited energy-selective capability of the detectors. The newer semiconductor detector systems have significantly greater energy resolution and thus provide greatly improved scatter rejection. This is often done, however, at some price in quantum efficiency.

Although the photon statistics are much poorer than that of radiography, the regions of interest can be delineated because of the greater contrast. For example, a brain lesion is difficult to detect radiographically since its attenuation coefficient differs only slightly from that of the surrounding tissue. As a result, the detection process requires large numbers of photons to reduce the standard deviation in the image. Conversely, in a nuclear medicine procedure the lesion takes up much more of the isotope than the surrounding tissue so that many fewer photons are required to distinguish the lesion.

Assuming that we have a source emitting a background level of n counts per unit area, the noise or standard deviation of the measurement is given by

$$\sigma = \sqrt{\frac{\eta}{M^2} nA} \tag{8.36}$$

where A is the area of a picture element in the image and $\eta n/M^2$ is the photon density at the image. The signal can be determined as in radiography, where C is the fractional difference between the photon density at the area of interest and the background resulting in a signal-to-noise ratio given by

$$\text{SNR} = C\sqrt{\frac{\eta}{M^2} nA}. \tag{8.37}$$

This assumes that the amplitude of the signal in the region of interest is unaffected by the blurring of the impulse response. A more accurate representation involves defining the image signal as the difference in the number of photons per element at the center of the lesion and in the background. We therefore convolve the image with the impulse response, as in equations (8.14) and (8.31), and evaluate the convolution at the center of the lesion. This is equivalent to taking the integral of the product of the image distribution and the impulse response centered at the center of the lesion. The difference between this value in photons per picture element and the background determines the signal.

The SNR is an interesting function of the aperture size in a pinhole imaging system. For example, assume that we are imaging a "cold" lesion such as occurs in the liver. This can be represented by a uniformly emitting area with a small nonemitting region representing the lesion. For a relatively small pinhole, the cold lesion is well resolved, so that the signal is equal to the background level since the value at the center of the lesion is zero. However, the low efficiency of

the small pinhole results in a low photon count and low SNR. As we increase the pinhole size, the photon count and SNR increases. However, at a certain aperture size, the lesion is no longer well resolved, so that the center of the lesion, due to convolution with the aperture function, is no longer zero. The reduced signal can then decrease the SNR. Clearly, there is an optimum size of pinhole aperture for each lesion size.

The system can be analyzed assuming a planar source distribution consisting of a background photon density $b(x, y)$ and a "lesion" density $l(x, y)$ centered at x_0, y_0 as given by

$$S(x, y) = b(x, y) + l(x - x_0, y - y_0). \tag{8.38}$$

The signal is defined as the magnitude of the difference in photons per pixel, between the center of the lesion and the background. The impulse response $h(x_d, y_d)$ is used to determine the response at each region as given by

$$\text{signal} = A \int\int h(x_d - Mx_0, y_d - My_0) l\left(\frac{x_d}{M} - x_0, \frac{y_d}{M} - y_0\right) dx_d dy_d \tag{8.39}$$

where A is the pixel area and M the magnification of the plane. The noise, as previously indicated, is the standard deviation of the background signal:

$$\text{noise} = \sqrt{A \int\int h(x_d, y_d) b\left(\frac{x_d}{M}, \frac{y_d}{M}\right) dx_d dy_d} \tag{8.40}$$

which, for $b(x, y)$ equal to a constant n photons per unit area, becomes $\sqrt{\eta n A / M^2}$.

CODED APERTURE SYSTEMS

In recent years there has been considerable research effort at imaging structures with increased capture efficiency as compared to the 10^{-4} of pinhole and parallel hole collimators. One approach is the use of an imaging structure consisting of an array of pinholes known as a coded aperture plate [Barrett, 1972; Barrett et al., 1972]. This structure, shown in Fig. 8.10, is used in place of the pinhole in a

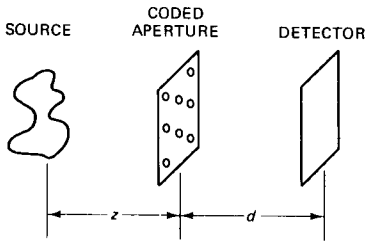

FIG. 8.10

nuclear medicine camera. The resultant coded image is thus the convolution of the source with that of the aperture plate. This image must then be decoded, by a suitably magnified version of the aperture plate, to reconstruct the object at any plane. Since the convolution is a function of the depth plane, three-dimensional information is derived. In addition, the average transmission of the aperture plate can be made many times greater than that of the pinhole. Using the same notation as the pinhole analysis, the detected intensity due to a source at plane z is given by

$$I_d = \frac{1}{4\pi d^2 m^2} S\left(\frac{x_d}{M}, \frac{y_d}{M}\right) ** a\left(\frac{x_d}{m}, \frac{y_d}{m}\right) \tag{8.41}$$

where $S(x, y)$ is the source distribution at plane z, $a(x, y)$ is the transmission of the aperture plate, and

$$M = -\frac{d}{z} \quad \text{and} \quad m = \frac{z + d}{z} = 1 - M. \tag{8.42}$$

In decoding the detected image, we cross correlate with the appropriately magnified version of the aperture plate to provide the reconstructed image as given by

$$I_r = I_d \star\star a\left(\frac{x_d}{m}, \frac{y_d}{m}\right) \tag{8.43}$$

$$= \frac{1}{4\pi d^2 m^2} S\left(\frac{x_d}{M}, \frac{y_d}{M}\right) ** \left[a\left(\frac{x_d}{m}, \frac{y_d}{m}\right) \star\star a\left(\frac{x_d}{m}, \frac{y_d}{m}\right)\right]. \tag{8.44}$$

The point response of the reconstructed image $h(x, y)$ is given by the autocorrelation of the aperture function as

$$h(x_d, y_d) = a\left(\frac{x_d}{m}, \frac{y_d}{m}\right) \star\star a\left(\frac{x_d}{m}, \frac{y_d}{m}\right). \tag{8.45}$$

Thus an aperture plate should be chosen which has a high-amplitude, narrow autocorrelation peak for good resolution and large open area for good efficiency. Examples are random pinhole arrays and Fresnel zone plates. The latter can be reconstructed optically since propagation through space provides the desired correlation function. A different magnification m is used for each depth plane so as to reconstruct each depth region separately.

This imaging structure exhibits good performance for small sources. For larger sources, however, comparable to the size of the coded aperture, the noise performance is considerably degraded. The basic problem arises from the nonnegative nature of the aperture function $a(x, y)$. Its autocorrelation, for an aperture containing a large number of holes, will consist of a narrow central peak having a normalized value of n, the number of holes, and a large background pedestal having a value of about unity, corresponding to the overlap of single holes in the autocorrelation. The convolution with this function essentially produces an image that is amplified by n, plus an integral of the image as a result of the large background pedestal of the function.

It is instructive to compare the signal-to-noise ratio of a single pinhole system to that of a coded aperture with n pinholes each having the same size. The signal-to-noise ratio of a uniform region using the single pinhole is given by

$$\mathrm{SNR}_{\text{pinhole}} = \frac{N}{\sqrt{N}} = \sqrt{N} \tag{8.46}$$

where N is the number of detected photons per picture element. In the multiple aperture plate the signal is given by nN because of the autocorrelation function. The variance is the sum of the noise due to the narrow peak in the autocorrelation and the integrated sum of the sources due to the large pedastal. Since these are independent, the variance is given by

$$(\text{variance})_{\text{multiple aperture}} = nN + mN \tag{8.47}$$

where m is the number of equal intensity sources. The resultant signal-to-noise ratio is given by

$$\mathrm{SNR}_{\text{multiple aperture}} = \frac{nN}{\sqrt{nN + mN}} = \frac{n\sqrt{N}}{\sqrt{n + m}}. \tag{8.48}$$

For small sources, where $n \gg m$, this becomes

$$\mathrm{SNR}_{\text{multiple aperture}} \simeq \sqrt{n}\sqrt{N} = \sqrt{n}\ \mathrm{SNR}_{\text{pinhole}} \tag{8.49}$$

where the improvement is obvious. For large sources $m \gg n$ the signal-to-noise ratio significantly deteriorates. For highly extended sources the resultant signal-to-noise ratio is poorer than that of the single pinhole so that the coded aperture system results in poorer noise performance. However, it continues to provide depth information which the single pinhole does not. Improved versions of these imaging systems are presently under study.

TOMOGRAPHIC SOURCE IMAGING

To avoid dealing with a projection of a volumetric object, tomographic systems are used to provide three-dimensional information. These have direct analogies with x-ray tomographic systems, so that we can rely heavily on the results of Chapter 7. For example, a simple motion tomography system can be created from the pinhole imaging system of Fig. 8.6 by moving the pinhole in a line pattern described by $f(x, y)$ with the detector moved in a magnified pattern $f(x/m, y/m)$. This will result in the image at plane z remaining in focus and the others being blurred by varying amounts.

As with radiography, motion tomography provides limited improvement since the intermediate planes are still present. Computerized tomography provides isolated sections of the three-dimensional volume completely free of intermediate structures [Budinger and Gullberg, 1974]. Here the data are acquired with a basic nuclear medicine camera, usually using a parallel hole collimator, moved around the patient to collect an array of projection images at many angles. These data are processed exactly as described in Chapter 7, where each measurement represents the line integrals of the sources at a particular angle. The reconstruction usually uses the convolution–back projection algorithm described in detail in Chapter 7. Because of the sensitivity of these reconstruction systems, it is particularly important to correct for attenuation so as to obtain the true line integrals of the source distribution. This can be accomplished by assuming a fixed value of μ as previously indicated. For greater accuracy, however, we can use an external source at the same energy as the isotope being imaged to provide a reconstruction of $\mu(x, y)$ using transmission computerized tomography. These values are then used to correct for the measured projections of the source distribution.

In nuclear medicine, using a parallel hole collimator, at each projection angle we simultaneously measure the projections of an array of planar sections. The complete reconstruction is therefore an array of continuous sections of the volume. A typical series of reconstructions of the brain is shown in Fig. 8.11.

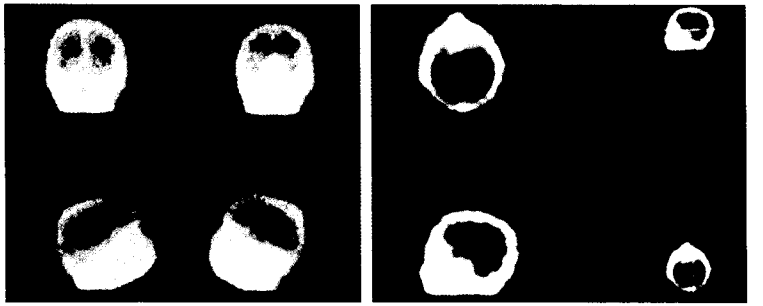

(a) (b)

FIG. 8.11 Conventional and cross-sectional reconstruction images of the brain. (Courtesy of the General Electric Medical Systems Division.)

In this study conventional projection images of the activity of the brain are compared to cross-sectional reconstruction. The patient had a lesion in the left temporal lobe which was not visible on the projection images. To provide the cross-sectional reconstruction, 64 views were acquired at a rate of 30 seconds per view. These were reconstructed and examined. The lesion appears on the transverse and sagittal sections shown. It is clear that in this case the projection images, representing the superimposed activity of all planes, failed to demonstrate the disease.

POSITRON IMAGING

Positron emitters generate a unique configuration of gamma rays. Each emitted positron almost immediately interacts with an electron to produce an annihilation event which generates two gamma rays each having energies of 510 kev and at almost exactly opposite directions [Meredith and Massey, 1977; Johns and Cunningham, 1974]. This phenomenon gives rise to a camera system shown in Fig. 8.12. Here a pair of two-dimensional position-indicating detectors are used

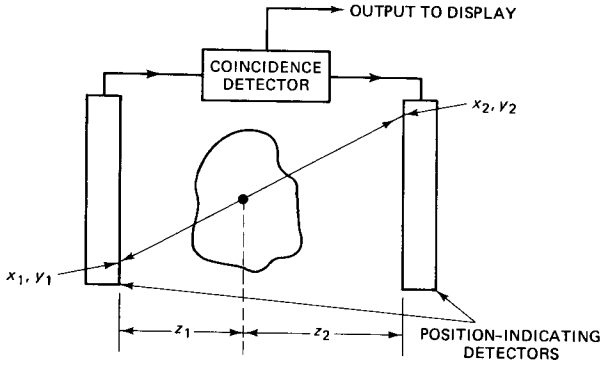

FIG. 8.12 Positron imaging system.

on either side of the subject. These can be either discrete arrays of detectors or Anger cameras as previously described. The energy-selective mechanisms of the detectors are set for 510 kev. When an annihilation event occurs, two photons travel to the individual detectors. A coincidence detector records an output event only in response to gamma rays being received at both detectors. This helps to eliminate various undesired events, such as Compton-scattered photons. Following a coincidence, the source position can be estimated for a known depth plane as given by

$$\hat{x} = \frac{x_1 z_2}{z_1 + z_2} + \frac{x_2 z_1}{z_1 + z_2}, \qquad \hat{y} = \frac{y_1 z_2}{z_1 + z_2} + \frac{y_2 z_1}{z_1 + z_2} \tag{8.50}$$

where x_1, y_1 and x_2, y_2 are the coordinates of the first and second detectors and z_1 and z_2 are the respective distances from the detectors to the source point. In general, a given plane of interest is studied so that the reconstruction is accurate in that plane and blurred for other planes as with motion tomography. The significant feature is that no collimators are required. The only limitation to the photon collection angle is the size of the detecting planes themselves.

One method of avoiding the blurring from other planes is to measure the difference of arrival time of the pair of photons and use that information to determine the source plane. Unfortunately, considering the velocity of light, it

would require 30-picosend accuracy to provide 1.0-cm-depth resolution. That is well beyond our present electronic capability, both in the detection and processing systems. This method does, however, have interesting potential for the future.

A recent exciting approach to the reconstruction, which avoids the overlap of planes, is the line integral technique discussed in Chapter 7 in the section on computerized tomography. If we sum up all the coincidence events reaching each pair of detector locations x_1, y_1 and x_2, y_2, we will have calculated the line integral of all the sources along that line. Having the line integral measurement over all angles and positions, we can then reconstruct the complete source distribution.

A system for accomplishing that specific task is the positron ring shown in Fig. 8.13 [Ter-Pogossian et al., 1975]. This system is used to reconstruct the

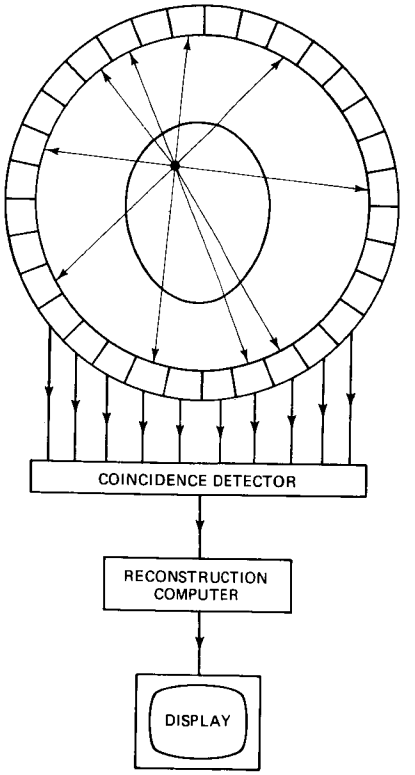

FIG. 8.13 Positron ring detector.

sources in a plane. The sum of coincident events in each detector pair around the ring represents the desired line integral. Since the line integral is available for a complete range of angles and positions, the reconstruction techniques used can be the same as those discussed in Chapter 7. The attenuation should again be considered, although, at these higher energies of 510 kev, it is somewhat less of a problem.

Positron imaging has two inherent limitations to its ultimate resolution. These are the range of the positron between its point of creation at the isotype and its point of annihilation, and the departure from 180° of the two photons because of the momentum of the positron. It should be emphasized, however, that in present systems the position detection accuracy, photon statistics, and sampling are the major limitations which provide a lateral resolution in the order of 1.0 cm. One practical difficulty in the use of these cameras is that many of the desirable isotopes must be produced by an on-site cyclotron. However, some of the resultant images represent outstanding delineations of perfusion and metabolism which are unavailable using other modalities.

PROBLEMS

8.1 In a pinhole source imaging system, the aperture $a(x, y) = \text{rect}(x/X)\ \text{rect}\ (y/Y)$. During the exposure the aperture center is translated from $x = -D_1/2$ to $x = D_1/2$ while the detector center is translated from $x_d = -D_2/2$ to $x_d = D_2/2$ in the same direction, where $D_2 > D_1$.

(a) At what plane is the image not degrated by the motions?

(b) Find the resultant recorded point response function $h(x_d, y_d)$ as a function of depth z.

8.2 A source consists of an infinite sheet of isotropically radiating material emitting n photons/unit area and has a nonemitting hole of radius a (Fig. P8.2). The source is imaged with a circular pinhole of radius b as shown using a pixel area A. The signal is defined as the difference in the number of photons per pixel between the background level of the image and the level at the center of the hole.

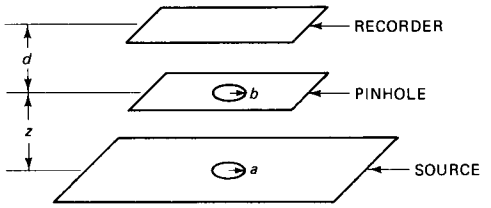

FIG. P8.2

(a) Find the signal-to-noise ratio versus b. [*Hint:* Use analytic expressions for two ranges of b.]

(b) Find the pinhole size that maximizes the signal-to-noise ratio.

8.3 A source consists of an infinite sheet of isotropically radiating material emitting n photons per unit area and has a nonemitting rectangular hole $D \times 2D$. The source is imaged with a $B \times B$ square pinhole a distance z from the source and d from the detector. The signal is defined as the difference in photons per pixel between the background and the center of the hole image. The area of a pixel is A.

(a) Calculate SNR versus B.

(b) Find the size of B for optimum SNR.

8.4 An infinite planar source having a photon emission density $n_0(1 + p \cos 2\pi f_0 x)$ is imaged using a pinhole system with a source to pinhole distance z and a pinhole to detector distance d. The signal is defined as the peak of the number of photons per pixel of the detected sinusoid. Assume a pixel area of A.

(a) Find an expression for the signal-to-noise ratio for a general aperture $a(x, y)$.

(b) For an aperture having a Gaussian transmission, $e^{-(r/b)^2}$, find the value of b that maximizes the signal-to-noise ratio.

8.5 The same source as in Problem 8.4 is imaged using a parallel hole collimator having a thickness L with circular holes of diameter D. Calculate the signal-to-noise ratio assuming that the impulse response is limited to the projection of a single hole.

8.6 As shown in Fig. P8.6, a pinhole imaging system of radius R is used to image a volumetric source distribution of thickness L, having a cylindrical

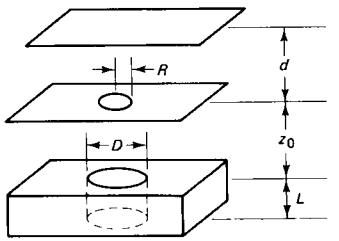

FIG. P8.6

hole of diameter D, where $D/2 > R$, and emitting n photons per unit volume. The signal is defined as the difference in photons per pixel of the background level and the center of the hole image. Assuming a pixel area of A, calculate the SNR versus z_0, the depth of the emitting source.

8.7 A parallel hole collimator has $D \times D$ square holes whose centers are separated by w in both dimensions, a thickness L with the detector plane a distance d from the top of the collimator. A planar source a distance z_0 from the bottom of the collimator has a distribution of $n_0[1 - \text{rect}\,(x/B)\,\text{rect}\,(y/B)]$ photons per unit area. Assume the hole separation is such that the impulse response at z_0 involves a single hole. Using the average impulse response and a pixel area of A, calculate the SNR.

9

Basic Ultrasonic Imaging

In this chapter the basic concepts of ultrasonic imaging [Wells, 1969; Woodcock, 1979] are introduced using a simplified model and some reasonable approximations. Although these simplifications and approximations lead to some inaccuracies, they do form the basis of most current medical ultrasonic imaging instruments.

This chapter is limited to the reflection imaging modality, where, as in radar, ultrasonic pulses are propagated through the body, causing reflected waves to occur at various discontinuities throughout the path of the propagated beam. Reflection or echo imaging is thus far the only one that has achieved commercial use. Other ultrasonic imaging modalities, which have thus far achieved only experimental use, are considered in Chapter 11.

This imaging modality is made possible by the relatively slow velocity of propagation of about 1500 meters/sec. This represents about a 333-μsec round trip time through 25 cm. In this time scale it is relatively simple for modern electronic circuitry to distinguish reflections at different depths with good resolution. This is in sharp distinction to the x-ray region, where the energy travels at the speed of light, 3×10^8 meters/sec. At these speeds it would require picosecond accuracies to distinguish various depths in the body. Current electronic techniques have not yet reached this capability. As a result, x-ray imaging, as has been described, is limited to the transmission modality.